MODELING THE DYNAMIC ELECTROMECHANICAL SUSPENSION BEHAVIOR OF AN ELECTRODYNAMIC EDDY CURRENT MAGLEV DEVICE

Nirmal Paudel[*] and Jonathan Z. Bird

Department of Electrical and Computer Engineering, University of North Carolina at Charlotte, 9201 University City Boulevard, Charlotte, NC 29223, USA

Abstract—A 2-D analytic based eddy-current transient model for a conducting plate is derived that is capable of accounting for continuous changes in the input conditions. Only the source field on the surface of the conducting plate needs to be known. In addition, a 2-D steady-state analytic based eddy-current model that is capable of accounting for frequency and velocity changes in two directions is derived. Both analytic based models have been validated using finite element code. The transient and steady-state models are integrated into an electromechanical system where the magnetic source is a Halbach rotor. The accuracy of both calculation methods is compared. The stiffness and damping coefficients are derived using the steady-state model.

1. INTRODUCTION

Most magnetic suspension (maglev) systems create suspension forces by either electromagnetic [1] or electrodynamic [2, 3] means. Both such methods typically involve translationally moving a magnetic source rapidly over a conductive surface. However, this motion gives rise to a large drag force. Various (costly) methods are used to reduce this drag force. An alternative is to try to use this drag force to create propulsion. This can be achieved by rotating a magnetic source rather than simply translationally moving it, as illustrated in Figure 1. The magnetic thrust force creation is analogous to an automobile wheel using frictional forces to create propulsion. The rotation of the magnets can create both a propulsion force in addition to suspension force [4, 5].
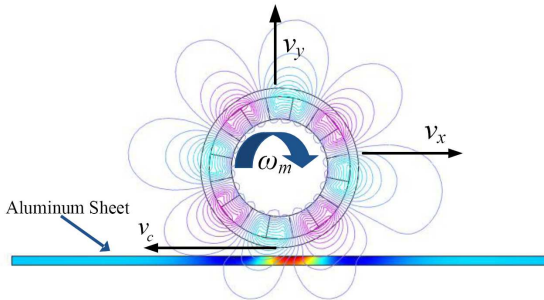
Figure 1. Finite element analysis model of a four pole-pair Halbach rotor rotating and translationally moving above an aluminum plate guideway. The field created by the Halbach rotor is shown as well as the induced guideway currents within the aluminum guideway plate.
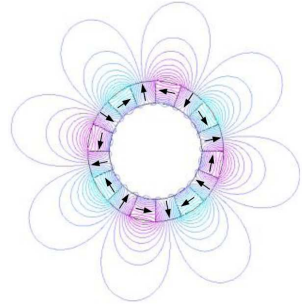

Figure 2. Field lines created by a four pole-pair Halbach rotor.

In order to create a large lift force a flux-focusing Halbach rotor [6–8], as shown in Figure 2, can be used.

If the relative velocity of the rotor, as seen by the conducting plate, is greater than the translational velocity, propulsion forces result, whereas if the rotor is rotated slower than the translational velocity braking forces are created [4, 5]. The use of a flat aluminum plate enables the normal forces to be used for suspension purposes. The slip, s_l, between the translational and rotational velocity is given by

$$s_l(t) = \omega_m(t)r_o - v_x(t) \tag{1}$$

where ω_m is the mechanical angular velocity, r_o the outer radius of the rotor, and v_x the translational velocity. The circumferential velocity v_c of the rotor is defined as

$$v_c(t) = \omega_m(t)r_o \tag{2}$$

The device shown in Figure 1 has been termed an electrodynamic wheel (EDW).

It is well known that electrodynamic suspension systems are highly underdamped [9]. Davis and Wilkie [10] analytically studied the dynamics of a long wire moving above a thin continuously uniform nonferromagnetic conducting plate while Baiko et al. [11] studied the dynamics using a rectangular coil. Both authors calculated that positive vertical damping is present at low-speeds while at high-speed the vertical damping can become negative. In contrast, Yoshida and Takakura [12] and Urankar [13] calculated that vertical damping is

always positive when a conducting coil is translationally moved above a conducting sheet. However, the damping values greatly reduce at high speed. Davis and Wilkie [10] and Yoshida and Takakura [12] calculated the forces utilizing a thin-sheet approximation approach in which the current is assumed to be constant throughout the plate thickness while Baiko et al. [11] and Urankar [13] accounted for current variation throughout the plate thickness.

Yamada et al. [14], Iwamoto et al. [15], Fujiwara [16], and Higashi et al. [17] calculated damping between translationally moving coils on a vehicle and stationary coils on a guideway. Iwamoto et al. used a lumped parameter based analysis while Fujiwara used a field based approach. They all concluded that the vertical magnetic damping becomes negative at medium and high speed, while Ooi [18], Takano and Ogiwara [19], Kratki and Oberretl [20], and He and Coffey [21] concluded the opposite. They used lumped parameter models to show that vertical magnetic damping was always positive but it decreased to very low values at high translational speeds.

The damping responses from experimental laboratory studies have been equally contradictory [9]. For instance, Zhu et al. [22] and Yamada et al. [14] performed vibration experiments using a rotating drum and a cantilevered magnet. They concluded that negative vertical damping occurred at high-speed, while Fujiwara [16] experimental results using superconducting magnets over guideway coils showed no negative damping at high speeds.

All researchers concluded that the inherent magnetic damping was insufficient and therefore active control of an electrodynamic maglev system is essential [9]. In this paper the dynamic response when a magnetic source has translational, vertical and rotational motion will be considered. The modeling characteristics when using two different formulation techniques for simulating the dynamics in an electromechanical eddy current device that utilizes a continuous linear finite thickness conducting plate will be presented. Exact electrodynamic stiffness and damping equations are derived.

2. FIELD BASED MODELING

The applicable quasi-static Maxwell's equations to model the problem shown in Figure 1 are [23, 24]

$$\nabla \times \mathbf{E} = -\frac{d\mathbf{B}}{dt} \tag{3}$$

$$\nabla \times \mathbf{B} = \mu_o \mathbf{J} \tag{4}$$

$$\nabla \cdot \mathbf{B} = 0 \tag{5}$$

$$\mathbf{J} = \sigma\mathbf{E} \tag{6}$$

$$\mathbf{B} = \nabla \times \mathbf{A} \tag{7}$$

$$\mathbf{E} = -\frac{d\mathbf{A}}{dt} - \nabla V \tag{8}$$

where $\mathbf{E}$ = electric field intensity (Vm^{-1}), $\mathbf{B}$ = magnetic flux density (Wbm^{-2}), μ_0 = permeability of free space (Hm^{-1}), $\mathbf{J}$ = current density (Am^{-2}), $\mathbf{A}$ = magnetic vector potential (Wbm^{-1}), σ = conductivity (Sm^{-1}) and V = electric scalar potential (V). Using the Coulomb gauge

$$\nabla \cdot \mathbf{A} = 0 \tag{9}$$

and assuming the conductive plate region is linear and simply connected then the governing transient eddy current field equation within a conductive plate can be described by [23]

$$\nabla^2\mathbf{A} = \mu_0\sigma\frac{d\mathbf{A}}{dt} \tag{10}$$

In general the vector potential can be a function of both position and time such that $\mathbf{A}(x(t), y(t), z(t), t)$. In this case the chain-rule can be applied to the time derivative term in (10) such that [25]

$$\frac{d\mathbf{A}}{dt} = \frac{\partial\mathbf{A}}{\partial t} + (\mathbf{v} \cdot \nabla)\mathbf{A} \tag{11}$$

where $\mathbf{v}$ is a velocity vector. Substituting (11) into (10) gives

$$\nabla^2\mathbf{A} = \mu_0\sigma\frac{\partial\mathbf{A}}{\partial t} + \mu_0\sigma(\mathbf{v} \cdot \nabla)\mathbf{A} \tag{12}$$

In this case the last term on the right side of (12) models the field's spatial change due to the position of the magnetic source while the first term on the right models changes in source field itself with respect to time.

Transient eddy current models are capable of accurately simulating the motion of complicated moving source fields. However, transient eddy-current simulations that utilize (10) or (12) can be very time intensive when incorporated into a dynamic mechanical system. This is especially so when there is continuous motion of the source field and there is a need for constant feedback between the eddy current force and the mechanical motion. In contrast, steady-state field based solutions can be solved much more quickly since the time variation is assumed to be [26]

$$\mathbf{A}(x, y, z, t) = \mathbf{A}(x, y, z)e^{j\omega_e t} \tag{13}$$

and therefore (12) reduces down to

$$\nabla^2\mathbf{A} = \mu_0\sigma(j\omega_e\mathbf{A} + (\mathbf{v} \cdot \nabla)\mathbf{A}) \tag{14}$$

Equation (14) can be calculated with relative ease when compared with the transient solution. The vast majority of steady-state models incorporate only one velocity term in the conducting region. Invariably this velocity term is in the direction of motion [24, 26, 27]. In this paper, the modeling accuracy will be considered when incorporating both a translational velocity, v_x, and a heave velocity, v_y, into an electromechanical transient simulation [28]. This study will be limited to a 2-D based analysis. However, the results and conclusions presented in this paper can be extended to 3-D based problems. For 2-D problems (10) and (14) reduce down to [5, 29, 30]

$$\nabla^2 A_z = \mu_0 \sigma \frac{\partial A_z}{\partial t} \tag{15}$$

$$\nabla^2 A_z = \mu_0 \sigma \left(j\omega_e A_z + v_x \frac{\partial A_z}{\partial x} + v_y \frac{\partial A_z}{\partial y} \right) \tag{16}$$

A 2-D solution is approximately accurate as long as the plate is sufficiently wide and the plate overhang width is significantly great [24]. Two different dynamic electromechanical simulations will be compared. The first model utilizes the coupled electromechanical system summarized in Figure 3 in which an analytic based *transient* eddy current formulation is coupled to a *transient* mechanical system. The electromagnetic forces, F_x, F_y are calculated using a *transient* electromagnetic model. In the second model, shown in Figure 4, a *steady-state* based eddy current model in which translational velocity, v_x, heave velocity, v_y, as well as rotational motion, ω_e, is accounted for is coupled to the *transient* mechanical model. The transient changes in vertical and horizontal position of the source are accounted for by feeding back the position and velocity terms determined from the mechanical model at each time step.

An analytic solution to (16) is derived in Section 3. This model is an extension of the 2-D model presented in [26]. In addition, the transient model for a step change developed in [31] is extended so as to be capable of accounting for continuous variations in the source conditions as derived in Section 4. Both the steady-state
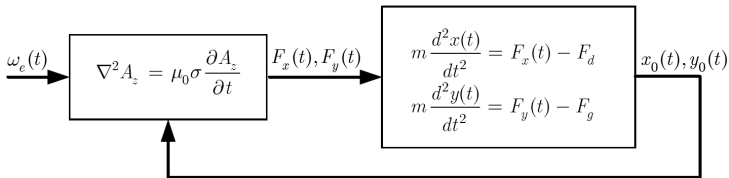
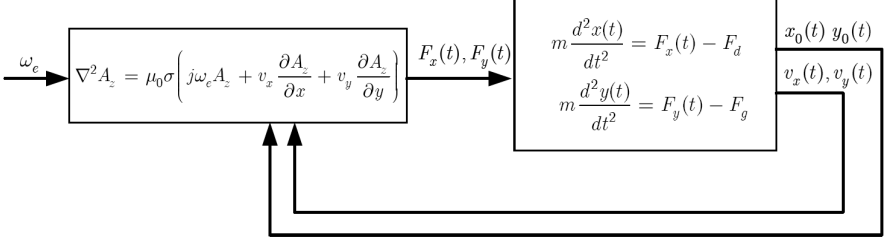

Figure 3. The formulation for transient model.
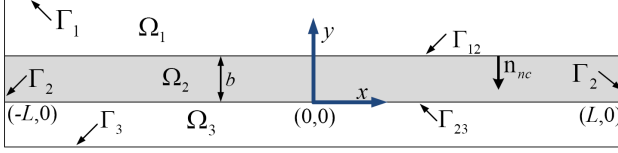
Figure 4. The formulation for a steady-state model.

Figure 5. Illustration of the conductive (Ω_2) and non-conductive (Ω_1, Ω_3) regions and boundaries used by the analytic based model. The conductive plate has a thickness of b.

and transient eddy current models are incorporated into the same mechanical model so that the accuracy of the steady-state model when coupled to a transient mechanical system can be assessed. The accuracy is compared by using the EDW source.

3. STEADY STATE MODEL

The 2-D problem region is illustrated in Figure 5. It consists of two non-conducting regions Ω_1, Ω_3 and a conducting region Ω_2. The conducting plate is of finite thickness, b and it is assumed to have a length that is significantly longer than the source field. A magnetic source (not shown) is assumed to be located only in region Ω_1.

3.1. Governing Equations and Boundary Conditions

The governing equation within the conducting region is given by (16). The source field, $\mathbf{B}^s$, and the reflected field, $\mathbf{B}^r$, due to the induced current in the non-conducting region Ω_1 and Ω_3 is

$$\mathbf{B}(x, y) = \mathbf{B}^s(x, y) + \mathbf{B}^r(x, y) \tag{17}$$

The reflected field can be further written in terms of the scalar potential, ϕ_n, defined as

$$\mathbf{B}^r = -\mu_0 \nabla \phi_n, \quad \text{in } \Omega_n \tag{18}$$

where $n = 1, 3$ for region 1 and region 3. Taking the divergence of (17) and since $\nabla \cdot \mathbf{B}^s = 0$ it can be noted that the non-conducting region can be modeled using

$$\frac{\partial^2 \phi_n}{\partial x^2} + \frac{\partial^2 \phi_n}{\partial y^2} = 0 \quad \text{in } \Omega_n. \tag{19}$$

By utilizing the scalar potential in Ω_1, Ω_3 the source term only needs to be accounted for on the conductive boundary [26, 32]. The boundary conditions for the electromagnetic fields at the top boundary interface between the non-conducting and conductive guideway regions, Γ_{12}, are

$$\mathbf{n}_{nc} \cdot (\mathbf{B}_1 - \mathbf{B}_2) = 0, \quad \text{on } \Gamma_{12} \tag{20}$$

$$\mathbf{n}_{nc} \times (\mathbf{H}_1 - \mathbf{H}_2) = 0, \quad \text{on } \Gamma_{12} \tag{21}$$

Since the permeability of the non-conducting and conducting regions is the same, the boundary condition (21) can be written as

$$\mathbf{n}_{nc} \times (\mathbf{B}_1 - \mathbf{B}_2) = 0, \quad \text{on } \Gamma_{12} \tag{22}$$

The field in the non-conducting region 1 is composed of a source field, $\mathbf{B}^s$ and an eddy current reflected field $\mathbf{B}^r$ defined as

$$\mathbf{B}_1 = \mathbf{B}^s + \mathbf{B}^r \tag{23}$$

The reflected field can be defined in terms of the scalar potential

$$\mathbf{B}^r = -\mu_0 \nabla \phi_1 \tag{24}$$

The field within the conductive region 2, the transmitted field, can be expressed in terms of a vector potential defined by

$$\mathbf{B}_2 = \nabla \times A_z^{ss} \tag{25}$$

Substituting (23) and (25) the boundary conditions on Γ_{12} can be written in terms of the vector and scalar field values such that [26, 33]

$$-\mu_0 \frac{\partial \phi_1}{\partial x} + B_x^s(x, b) = \frac{\partial A_z^{ss}}{\partial y}, \quad \text{on } \Gamma_{12} \tag{26}$$

$$\mu_0 \frac{\partial \phi_1}{\partial y} - B_y^s(x, b) = \frac{\partial A_z^{ss}}{\partial x}, \quad \text{on } \Gamma_{12} \tag{27}$$

Similarly, when there is no source in region 3 the boundary conditions on Γ_{12} are

$$-\mu_0 \frac{\partial \phi_3}{\partial x} = \frac{\partial A_z^{ss}}{\partial y}, \quad \text{on } \Gamma_{23} \tag{28}$$

$$-\mu_0 \frac{\partial \phi_3}{\partial y} = -\frac{\partial A_z^{ss}}{\partial x}, \quad \text{on } \Gamma_{23} \tag{29}$$

where $B_x^s(x, b)$, $B_y^s(x, b)$ are the magnetic source terms. The source field is centered at $x = 0$. On the outer non-conducting boundaries

$\phi_1 = 0$ on Γ_1 and $\phi_3 = 0$ on Γ_3. In this paper, the source is assumed to be only located in Ω_1 therefore it is only present in boundary condition (26) and (27). However, this method can be used in a situation when a source is presented on both the top and the bottom surfaces. In that case, boundary conditions (28) and (29) will have an extra source terms similar to (26) and (27).

3.2. Fourier Solution of Governing Equations

The governing Equations (16) and (19) must satisfy the boundary conditions (26)–(29) and outer boundary requirements. The solution of this problem has been obtained by using the spatial Fourier transform technique [34] in which the Fourier transform for the vector and scalar potential regions with respect to the x-axis are

$$A_z^{ss}(\xi, y) = \int_{-\infty}^{\infty} A_z^{ss}(x, y)e^{-j\xi x}dx \tag{30}$$

$$\phi_n(\xi, y) = \int_{-\infty}^{\infty} \phi_n(x, y)e^{-j\xi x}dx. \tag{31}$$

By utilizing (30), (16) reduces to

$$\frac{\partial^2 A_z^{ss}(\xi, y)}{\partial y^2} - 2\lambda\frac{\partial A_z^{ss}(\xi, y)}{\partial y} - \gamma^2 A_z^{ss}(\xi, y) = 0, \quad \text{in } \Omega_2 \tag{32}$$

where

$$\gamma^2 = \xi^2 + \mu_0\sigma s_0 \tag{33}$$
$$s_o = j(\omega_{eo} + \xi v_{xo}) \tag{34}$$
$$\lambda = \frac{v_y\mu_0\sigma}{2} \tag{35}$$

Solving (32) gives the general solution in Ω_2 as

$$A_z^{ss}(\xi, y) = \left[M(\xi)e^{y\beta} + N(\xi)e^{-y\beta}\right]e^{y\lambda} \tag{36}$$

where

$$\beta^2 = \lambda^2 + \gamma^2 \tag{37}$$

and $M(\xi)$ and $N(\xi)$ are unknowns. The Fourier transform of (19) is

$$\frac{\partial^2 \phi_n(\xi, y)}{\partial y^2} = \xi^2\phi_n(\xi, y), \quad \text{in } \Omega_n \tag{38}$$

where $n = 1$ and 3. Solving (38) and noting that when moving away from the plate along the y-axis in Ω_1 and Ω_3 the field must reduce to zero one obtains the solutions

$$\phi_1(\xi, y) = X_1(\xi)e^{-\xi y}, \quad \text{in } \Omega_1 \tag{39}$$

$$\phi_3(\xi, y) = X_3(\xi)e^{\xi y}, \quad \text{in } \Omega_3 \tag{40}$$

where $X_1(\xi)$ and $X_3(\xi)$ are unknowns. The boundary conditions (26)–(29) are Fourier transformed with respect to x and (36), (39) and (40) are substituted into the transformed boundary conditions. Solving for the unknowns $M(\xi)$ and $N(\xi)$ enables the magnetic vector potential to be derived as

$$A_z^{ss}(\xi, y) = T^{ss}(\xi, y)B^s(\xi, b) \tag{41}$$

where

$$T^{ss}(\xi, y) = \frac{\left[[\lambda - (\xi + \beta)]e^{\beta y} - [\lambda - (\xi - \beta)]e^{-\beta y}\right] e^{\lambda(y-b)}}{e^{\beta b}[\lambda^2 - (\xi + \beta)^2] - e^{-\beta b}[\lambda^2 - (\xi - \beta)^2]} \tag{42}$$

can be interpreted as the transmission function for an arbitrary source field, $B^s(\xi, b)$, imparted on the plate surface, Γ_{12}. The $B^s(\xi, b)$ source field is

$$B^s(\xi, y) = B_x^s(\xi, y) + jB_y^s(\xi, y) \tag{43}$$

The reflected field can be determined by solving for $X_1(\xi)$, from which it is determined that [31, 33]

$$B_y^r(\xi, y) = jB_x^r(\xi, y) \tag{44}$$

where

$$B_y^r(\xi, y) = \left[B_y^t(\xi, b) - B_y^s(\xi, b)\right] e^{\xi(b-y)} \tag{45}$$

and the transmitted field $B_y^t(\xi, y)$ is

$$B_y^t(\xi, y) = -\frac{\partial A_z^{ss}(\xi, y)}{\partial x} = -j\xi T^{ss}(\xi, y)B^s(\xi, b) \tag{46}$$

The transmitted, reflected and source fields at the boundary, $y = b$, are therefore

$$B_y^t(\xi, b) = B_y^r(\xi, y) + B_y^s(\xi, b) \tag{47}$$

$$B_x^t(\xi, b) = B_x^r(\xi, y) + B_x^s(\xi, b) \tag{48}$$

3.3. Force Calculation

The forces are calculated by evaluating the stress tensor equation on Γ_{12} ($y = b$). Due to Parseval's theorem the force integration can be

evaluated in the Fourier domain thereby avoiding the need to first obtain the inverse transform [29, 35]. The thrust and lift forces are

$$F_x = \frac{w}{4\pi\mu_0}\text{Re}\int_{-\infty}^{\infty} B_x^{t*}B_y^t d\xi \tag{49}$$

$$F_y = \frac{w}{8\pi\mu_0}\text{Re}\int_{-\infty}^{\infty} \left(B_y^{t*}B_y^t - B_x^{t*}B_x^t\right)d\xi \tag{50}$$

where star-superscript denotes complex conjugation. After substituting (47), (48) into (49), (50) it can be shown that for an arbitrary source the force equations are given by [31, 33]

$$F^{ss} = \frac{w}{8\pi\mu_0}\int_{-\infty}^{\infty} [2\xi A_z(\xi,b)B^{s*}(\xi,b) - |B^s(\xi,b)|^2]d\xi, \quad \text{on } \Gamma_{12} \tag{51}$$

where the normal, F_y, and tangential force, F_x, on the rotor are

$$F^{ss} = F_y + jF_x \tag{52}$$

Therefore

$$F_x = -\text{Im}[F^{ss}] \tag{53}$$

$$F_y = -\text{Re}[F^{ss}] \tag{54}$$

Based on convention lift force is defined as a positive force and therefore the negative signs in (53) and (54) ensures that both lift and thrust force are the force acting on the rotor source. The force equation given by (51) can be further simplified. Substituting (41) into (51) and rearranging gives

$$F^{ss} = \frac{w}{8\pi\mu_0}\int_{-\infty}^{\infty} \Gamma(\xi,b)|B^s(\xi,b)|^2 d\xi, \quad \text{on } \Gamma_{12} \tag{55}$$

where

$$\Gamma(\xi,b) = 2\xi T^{ss}(\xi,b) - 1 \tag{56}$$

$$= \frac{\mu_0\sigma[s_o - v_y\xi]}{2\xi^2 + \mu_0\sigma s_o + 2\beta\xi\coth(\beta b)} \tag{57}$$

4. TRANSIENT EDDY CURRENT MODEL FOR AN ARBITRARILY CHANGING SOURCE

In [31, 33] the 2-D transient eddy current forces due to a step change in angular velocity and/or translational velocity of a source field above

a linear conductive plate were derived. The model was validated by comparing it with finite element analysis (FEA) code. Unlike with the steady-state model, the motional effects are accounted for by moving the source field. The model is capable of predicting transient force changes given an initial steady-state condition. In order to be coupled to a dynamic electromechanical model the transient eddy-current model must be capable of predicting forces for continuous changes in operating inputs from non-steady state initial conditions. In this section the model presented in [31] is extended to model continuous changes in the source input. The Fourier and Laplace transformed solution for the vector potential in Ω_2, for the case when $A_z(x, y) = 0$ at $t = 0$ is [31]

$$A_z^{tr}(\xi, y, s) = T^{tr}(\xi, y, s) B^s(\xi, b, s) \tag{58}$$

The superscript tr stands for transient. The transmission function for the transient case is

$$T^{tr}(\xi, y, s) = \frac{(\alpha + \xi)e^{\alpha y} + (\alpha - \xi)e^{-\alpha y}}{e^{\alpha b}(\alpha + \xi)^2 - e^{-\alpha b}(\alpha - \xi)^2} \tag{59}$$

and

$$\alpha^2 = \xi^2 + \mu_0 \sigma s. \tag{60}$$

4.1. Vector Potential Step and Impulse Response

If the source field is a unit-step

$$B^s(\xi, b, t) = \frac{1}{s} \tag{61}$$

then by using (58) and following the derivation method given in [31] the vector potential field at $y = b$ is

$$A_z^{step}(\xi, b, t) = A_1 u(t) + \sum_{n=0}^{9} \left(A_t^n e^{s_t^n t} + A_c^n e^{s_c^n t} \right) \tag{62}$$

where $u(t)$ denotes the unit step function. In (62) only the first 10 roots of cot and tan are evaluated numerically and the root index is denoted by the superscript $n = 0, 1, \ldots 9$. The other variables in (62) are

$$A_1 = T(\xi, b, 0) = 1/(2\xi) \tag{63}$$

$$A_t^n = -\frac{8k_t^n}{\mu_o \sigma b^3 \xi^2} \frac{(2k_t^n \cot(2k_t^n) + b\xi)}{s_t^n \left(-\lambda k_t^n + \cot(k_t^n)\right)\left(\lambda + \sec^2(k_t^n)\right)} \tag{64}$$

$$A_c^n = \frac{8k_c^n}{\mu_o \sigma b^3 \xi^2} \frac{(2k_c^n \cot(2k_c^n) + b\xi)}{s_c^n \left(\lambda + \csc^2(k_c^n)\right)\left(\lambda k_c^n + \tan(k_c^n)\right)} \tag{65}$$

and the time constants are

$$s_q^n = -\left[\left(\frac{2k_q^n}{b}\right)^2 + \xi^2\right]\frac{1}{\mu_o\sigma} \tag{66}$$

where the subscript $q = t$ or c denotes the root solutions for the tan and cot terms. The impulse response can be obtained from the step response solution. Laplace transforming (62) and multiplying through by s gives

$$A_z^{imp}(\xi, b, s) = A_1 + \sum_{n=0}^{9}\left(\frac{A_t^n s}{s - s_t^n} + \frac{A_c^n s}{s - s_c^n}\right) \tag{67}$$

inverse Laplace transforming (67) one obtains

$$A_z^{imp}(\xi, b, t) = A_1\delta(t) + \sum_{n=0}^{9}\left(A_t^n + A_c^n\right)\delta(t) + \sum_{n=0}^{9}\left(A_t^n s_t^n e^{s_t^n t} + A_c^n s_c^n e^{s_c^n t}\right) \tag{68}$$

where $\delta(t)$ is the unit impulse function.

The transient response due to an arbitrary source change $B^s(\xi, b, \tau)$ at any point in time can be obtained by utilizing the convolution integral of the impulse response [36]

$$A_z(\xi, b, t) = \int_0^t B^s(\xi, b, \tau)A_z^{imp}(\xi, b, t - \tau)d\tau \tag{69}$$

substituting (68) into (69) gives

$$\begin{aligned}A_z^{tr}(\xi, b, t) &= \int_0^t B^s(\xi, b, \tau)\left[\left(A_1 + \sum_{m=0}^{9}\left(A_t^n + A_c^n\right)\right)\delta(t - \tau)\right.\\ &\left. + \sum_{n=0}^{9}\left(A_t^n s_t^n e^{s_t^n(t-\tau)} + A_c^n s_c^n e^{s_c^n(t-\tau)}\right)\right]d\tau. \tag{70}\end{aligned}$$

The x and y-component flux density transient response can be derived from the derivative of (70) [33].

4.2. Force Calculations

The transient forces can be computed using [31, 33]

$$F^{tr}(t) = \frac{w}{8\pi\mu_0}\int_{-\infty}^{\infty}[2\xi A_z(\xi, b, t)B^{s*}(\xi, b, t) - |B^s(\xi, b, t)|^2]d\xi, \quad \text{on } \Gamma_{12} \tag{71}$$

such that the normal and tangential force will be

$$F^{tr}(t) = F_y + jF_x \tag{72}$$

The accuracy of this transient eddy current model was validated with an FEA model [33]. The validation is provided in the Appendix.

5. HALBACH ROTOR SOURCE FIELD

The field results derived in Sections 3 and 4 can be utilized with any source term. Only the Fourier transformed field value on the surface of the conducting plate must be specified. In this analysis the source field is assumed to be a Halbach rotor that can simultaneously rotate and move in the x, y plane above the conductive plate. The coordinate system for such a Halbach rotor is shown in Figure 6. The center of the Halbach rotor is located at (x_o, y_o). The rotation frequency is assumed to be at a single frequency, $\omega_e(t)$, but its value however can change with time. The electrical and mechanical angular velocity, $\omega_m(t)$, are related by $\omega_e(t) = \omega_m(t)P$ where P is the number of pole-pairs. An airgap, g, between the rotor and conducting plate is always assumed.
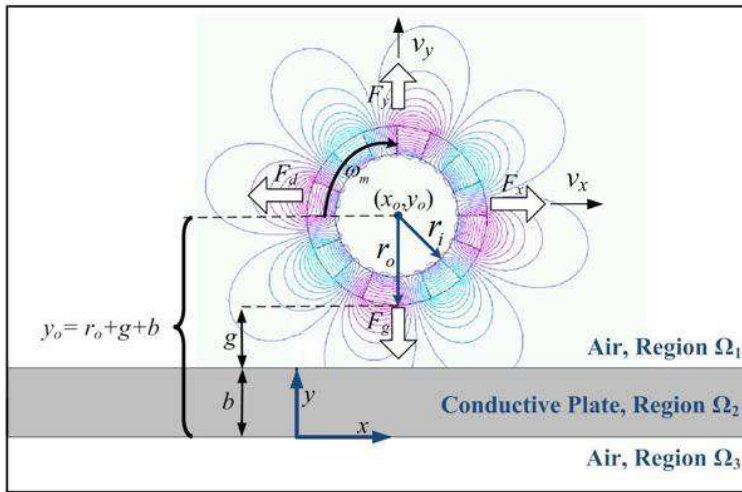

Figure 6. Coordinate system for Halbach rotor position above a conductive plate.

5.1. Transient Source Equation

The 2-D Halbach rotor field in air was derived in [37]. It can be expressed in vector potential form as

$$A_z^s(r, \theta, t) = \frac{C}{P} \frac{e^{jP\theta}}{r^P} e^{jP\omega_m t} \tag{73}$$

where

$$C = \left(\frac{2B_r P}{P+1} \right) \frac{(1+\mu_r)r_o^{2P}(r_o^{P+1} - r_i^{P+1})}{(1-\mu_r)^2 r_i^{2P} - (1+\mu_r)^2 r_o^{2P}} \tag{74}$$

B_r = magnet remanence, r_i = inner rotor radius and μ_r = relative permeability. The magnet eddy-current losses are neglected in the analysis but as the Halbach magnets are highly segmented, these losses will be relatively low [38]. The Halbach rotor's coordinate axis is located at (x_o, y_o) where

$$y_o = b + g + r_o \tag{75}$$

Using the complex analysis conversion [26, 33]

$$\frac{e^{jP\theta}}{r^P} = \frac{1}{(x_o - jy_o)^P} \tag{76}$$

and converting (73) to the conducting plate Cartesian coordinate reference frame gives

$$A_z^s(x, y, t) = \frac{Ce^{jP\omega_m t}}{P[(x-x_o) - j(y-y_o)]^P} \tag{77}$$

The translational source velocity term, v_x can also be included into (77). After including this, the source field flux density is given by

$$B_y^s(x, y, \omega_m, v_x, t) = -\frac{\partial A_z}{\partial x} = \frac{C}{[(x-v_xt-x_o)-j(y-y_o)]^{P+1}} e^{jP\omega_m t} \tag{78}$$

$$B_x^s(x, y, t) = jB_y^s(x, y, t) \tag{79}$$

Equations (78), (79) are utilized in the transient solution. The Fourier transformed transient source solution at $y = b$ is given by [26]

$$B_x^s(\xi, b, t) = (-j)^P \frac{2}{P!} C\pi\xi^P e^{-\xi(g+r_o+jx_o)} e^{j(P\omega_m - \xi v_x)t} u(\xi) \tag{80}$$

$$B_y^s(\xi, b, t) = -jB_x^s(\xi, b, t) \tag{81}$$

and the source equation defined by (43) for a Halbach rotor is then given by

$$B^s(\xi, b, t) = 2(-j)^P \frac{2}{P!} C\pi\xi^P e^{-\xi(g+r_o+jx_o)} e^{j(P\omega_m - \xi v_x)t} u(\xi) \tag{82}$$

5.2. Steady-state Source Equation

In the steady-state formulation the oscillating source frequency, ω_e, as well as both the translational and heave velocity terms are accounted for within the conducting plate solution given by (41). Therefore, the steady-state source equation used in (41) is [26, 33]

$$B_y^s(x, y) = -\frac{\partial A_z}{\partial x} = \frac{C}{[x - x_o - j(y - y_o)]^{P+1}} \tag{83}$$

$$B_x^s(x, y) = j B_y^s(x, y) \tag{84}$$

Substituting (83) and (84) into (43) and taking the Fourier transform gives the steady-state source solution at $y = b$ as

$$B^s(\xi, b) = \frac{4\pi C \xi^P}{P!} e^{-\xi(r_o + g + jx_o)} u(\xi). \tag{85}$$

Equation (85) was used in (41).

6. TWO DEGREE OF FREEDOM VEHICLE SIMULATION

In order to understand the impact on the electromechanical dynamic characteristics when the eddy current forces are calculated using the steady-state force model, a 2-degree of freedom electromechanical model comparison has been made. An electromechanical model using four EDWs has been created in the *Matlab-Simulink* environment. Each EDW is connected to the vehicle through a drive shaft. The traction motors have not been modeled. The torque is directly applied to the drive shafts. The basic configuration of the 'vehicle' is shown in Figure 7 and the block diagram for the integration of the wheel and vehicle model is shown in Figure 8. The parameters used by this model are given in Table 1. The selection between the transient and steady state eddy-current model is achieved by changing the
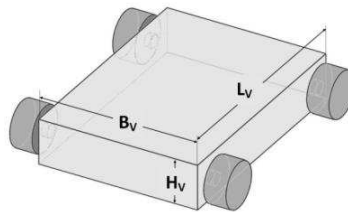

Figure 7. The maglev vehicle used for simulation where B_v, H_v and L_v are the breadth, height and length of the vehicle.
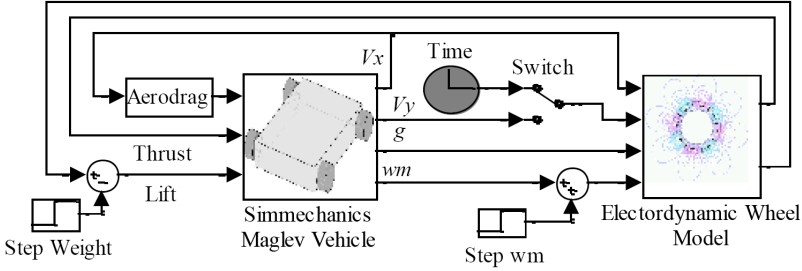
Figure 8. Block diagram showing the electrodynamic wheel and (mechanical) vehicle coupling. The steady state model includes v_y while the transient model includes the time.

position of the switch (in Figure 8). Only the variation in the vehicle height, y_o, in the y-axis, and translational position, x_o along the x-axis is considered. The vehicle's x and y-axis motion acts like an electromechanical nonlinear spring-mass system [39]. The governing mechanical equations are

$$m\frac{d^2y(t)}{dt^2} = F_y(t) - F_g(t) \tag{86}$$

$$m\frac{d^2x(t)}{dt^2} = F_x(t) - F_d(t) \tag{87}$$

where F_g = gravitational force and m = mass of vehicle and the rotor magnets. $F_x(t)$ and $F_y(t)$ are the thrust and lift force respectively. The aerodynamic drag force, $F_d(t)$, is given by [40]

$$F_d(t) = 0.5\rho C_d A v_x(t)^2 \tag{88}$$

where, ρ = density of air, C_d = aerodynamic drag coefficient, A = frontal area of the vehicle. No aerodynamic damping in y-direction is included. The values were chosen to match an experimental setup. The 'vehicle' was started with initial conditions: $10\,\text{ms}^{-1}$ translational velocity, $0\,\text{ms}^{-1}$ heave velocity, airgap $g = 10\,\text{mm}$, $\omega_m = 400\,\text{rads}^{-1}$. These initial conditions result in a positive slip $s_l = 10\,\text{ms}^{-1}$. The response when using these initial conditions with the steady-state model (given in Section 3) and transient model (Section 4) are compared in Figure 9 and Figure 10. Both use the same mechanical model. The large initial transient is due to the positive slip of the vehicle creating a thrust and lift force and consequently acceleration in the x and y direction at $t = 0\,\text{s}$. One can note that the steady-state model tracks the transient response quite closely. This is because of the presence of the v_y term in (16). The sudden change in lift force
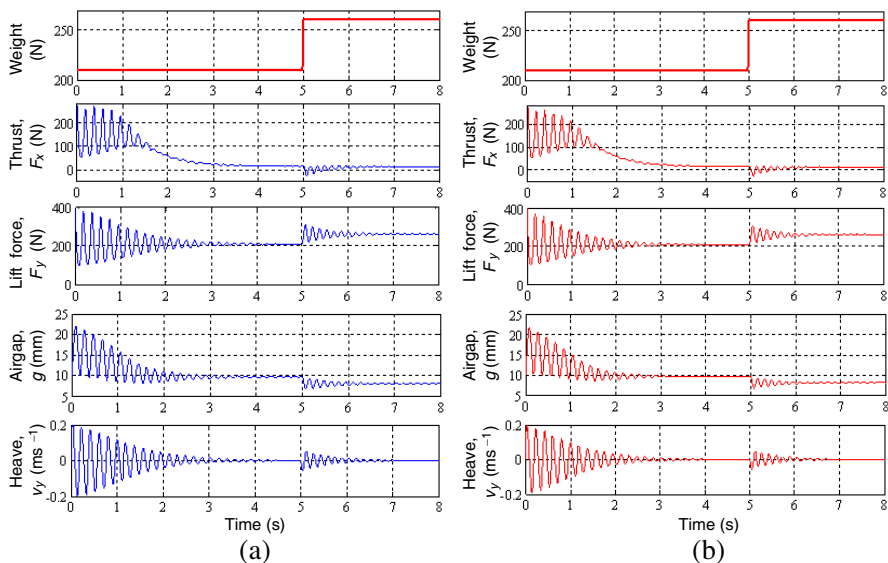
Figure 9. Simulation response when a step change in maglev vehicle weight of 50 N occurs at $t = 5$ s. The resulting response when (a) the transient eddy current model is used and (b) the steady-state eddy current model is used is shown. The thrust, lift, air-gap variation and heave velocity have been plotted.
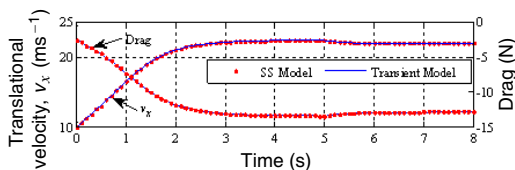

Figure 10. Translational velocity, v_x and aerodynamic drag force for a step change in weight.
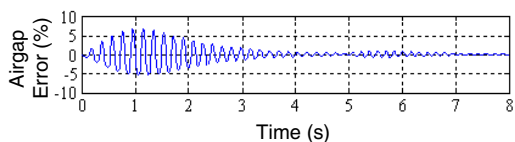

Figure 11. Percentage error between the steady state and transient eddy current electromechanical system for the airgap as a function of time.

Table 1. Dynamic simulation parameters.

	Description	Value	Units
Vehicle	Length of the vehicle, L_V	40	cm
	Breadth of the vehicle, B_V	20	cm
	Height of the vehicle, H_V	10	cm
	Thickness of vehicle, T_V	4	cm
	Frontal area of the vehicle, A	0.0476	m^2
	Density of iron, ρ_{Fe}	7.93	g/cm^3
	Length of drive shaft, L_{DS}	4	cm
	Radius of drive shaft, R_{DS}	1	cm
	Total mass of vehicle, m	21.38	kg
	Aerodynamic drag coefficient, C_d	0.25	kgs^{-1}
Halbach rotor	Outer radius, r_o	50	mm
	Inner radius, r_i	34.20	mm
	Width, w	50	mm
	Magnet (NdFeB), B_r	1.42	T
	Magnet relative permeability, μ_r	1.08	-
	Pole-pairs, P	4	-
Conducting plate	Conductivity (Al), σ	2.459×10^7	Sm^{-1}
	Single sheet width, ω	50	mm
	Thickness, b	10	mm
	Air-gap between rotor and plate, g	10	mm

creates a mechanical acceleration and consequently this is captured by the v_y term, without the feedback created by v_y the steady-state model cannot account for the dynamic variation in the airgap, g. The resulting error in airgap estimation is relatively small, as shown in Figure 11. Electromagnetic damping is clearly present. The lift and thrust forces are highly coupled. The translational velocity is smoothly increasing because the conducting plate is assumed to be infinitely uniform in the x-axis. At time $t = 5$ s a step change in mass occurs and this results in a second transient phase; again the electromechanical system with steady-state forces closely tracks the transient eddy-current electromechanical model.

A comparison for a step change in angular velocity is shown in Figure 12 and Figure 13. The model starts in a steady-state condition and then a step change in ω_m from 400 to 600 rads^{-1}

occurs at $t = 1\,$s. This results in an increased slip and consequently an increase in translational velocity. As the velocity is greater the new steady-state airgap value increases. The steady-state coupled electromechanical model again closely tracks the eddy-current based transient electromechanical model.
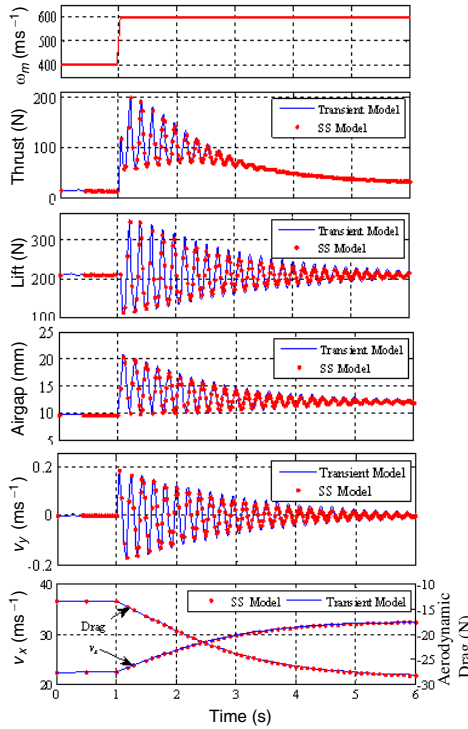

Figure 12. Electromechanical simulation results for a step change in angular velocity when using the stead-state and transient eddy current model.
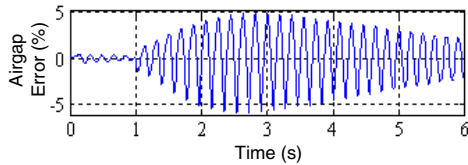

Figure 13. Percentage error between the steady state and transient eddy current electromechanical system for the airgap as a function of time.

7. STIFFNESS AND DAMPING ANALYSIS

The two degree freedom vehicle simulation results indicate that the eddy current damping and stiffness characteristics of the electromechanical system can be relatively accurately predicted by using (16). Therefore, as the steady-state equations are significantly simpler to understand and greatly faster to compute they have been used to study the stiffness and damping characteristics for this system. The magnetic damping coefficients are dependent on the transmission functions. The damping coefficient is defined as the negative derivative of force with respect to the velocity [41]. Differentiating (55) with respect to velocities in the x and y directions, one obtains

$$
\begin{bmatrix} D_{xx} & D_{xy} \\ D_{yx} & D_{yy} \end{bmatrix} = \begin{bmatrix} -\frac{dF_x}{dv_x} & -\frac{dF_x}{dv_y} \\ -\frac{dF_y}{dv_x} & -\frac{dF_y}{dv_y} \end{bmatrix} = \begin{bmatrix} \mathrm{Im}\left[\frac{dF^{ss}}{dv_x}\right] & \mathrm{Im}\left[\frac{dF^{ss}}{dv_y}\right] \\ \mathrm{Re}\left[\frac{dF^{ss}}{dv_x}\right] & \mathrm{Re}\left[\frac{dF^{ss}}{dv_y}\right] \end{bmatrix} \tag{89}
$$

The velocities, v_x and v_y in (89), are the velocities of the rotor and the damping forces are computed on the vehicle rather than the conductive plate. The derivative terms in (89) can be further written as

$$
\frac{dF^{ss}}{dv_x} = \frac{w}{8\pi\mu_0} \int_{-\infty}^{\infty} \frac{\partial\Gamma(\xi,b)}{\partial v_x} |B^s(\xi,b)|^2 d\xi \tag{90}
$$

$$
\frac{dF^{ss}}{dv_y} = \frac{w}{8\pi\mu_0} \int_{-\infty}^{\infty} \frac{\partial\Gamma(\xi,b)}{\partial v_y} |B^s(\xi,b)|^2 d\xi \tag{91}
$$

The derivatives of the transmission function in (90) and (91) are evaluated analytically and are determined to be

$$
\frac{\partial\Gamma(\xi,b)}{\partial v_x} = -j\mu\sigma\xi^2 \frac{\begin{array}{c}(\gamma^2 + 2\lambda(\lambda-\xi) + \xi^2)\coth(b\beta) \\ +2\beta(\xi-\lambda) + b\beta(\gamma^2 + 2\xi\lambda - \xi^2)\mathrm{csch}(b\beta)^2\end{array}}{\beta[2\xi\varsigma\coth(b\varsigma) + \gamma^2 + \xi^2]^2} \tag{92}
$$

$$
\frac{\partial\Gamma(\xi,b)}{\partial v_y} = \xi\mu\sigma \frac{\begin{array}{c}(\gamma^2(2\xi-\lambda) + \lambda\xi^2)\coth(b\beta) + \beta(\gamma^2 + \xi^2) \\ +b\lambda\beta(\gamma^2 + 2\xi\lambda - \xi^2)\mathrm{csch}(b\beta)^2\end{array}}{\beta[2\xi\varsigma\coth(b\varsigma) + \gamma^2 + \xi^2]^2}. \tag{93}
$$

The stiffness coefficient is defined as the negative derivative of forces with respect to the displacement [41]. The stiffness matrix for 2D model can be obtained by taking the derivative of force with respect to the x and y-axis displacements as given by

$$
\begin{bmatrix} k_{xx} & k_{xy} \\ k_{yx} & k_{yy} \end{bmatrix} = \begin{bmatrix} -\frac{dF_x}{dx_o} & -\frac{dF_x}{dy_o} \\ -\frac{dF_y}{dx_o} & -\frac{dF_y}{dy_o} \end{bmatrix} \tag{94}
$$

Using (52), (94) can be written as

$$
\begin{bmatrix} k_{xx} & k_{xy} \\ k_{yx} & k_{yy} \end{bmatrix} = \begin{bmatrix} \mathrm{Im}\left[\frac{dF^{ss}}{dx_o}\right] & \mathrm{Im}\left[\frac{dF^{ss}}{dy_o}\right] \\ \mathrm{Re}\left[\frac{dF^{ss}}{dx_o}\right] & \mathrm{Re}\left[\frac{dF^{ss}}{dy_o}\right] \end{bmatrix} \tag{95}
$$

Assuming that the complex force function (52) has a derivative over all space then it can be said that (52) is analytic and therefore the Cauchy-Riemann equation is applicable. The Cauchy-Riemann equation states that [42]:

$$
\frac{\partial F_y}{\partial x_o} = \frac{\partial F_x}{dy_o} \tag{96}
$$

$$
\frac{\partial F_y}{\partial y_o} = -\frac{\partial F_x}{dx_o} \tag{97}
$$

Equation (97) is the 2-D form of Earnshaw's theorem [43–45]. Substituting (96) and (97) into (95), the stiffness matrix becomes

$$
\begin{bmatrix} k_{xx} & k_{xy} \\ k_{yx} & k_{yy} \end{bmatrix} = \begin{bmatrix} -\mathrm{Re}[\frac{dF^{ss}}{dy_o}] & \mathrm{Im}[\frac{dF^{ss}}{dy_o}] \\ \mathrm{Im}[\frac{dF^{ss}}{dy_o}] & \mathrm{Re}[\frac{dF^{ss}}{dy_o}] \end{bmatrix} \tag{98}
$$

When the source field is given by (85) it can be noted that the airgap, g, will be changing therefore

$$
\frac{dF^{ss}}{dy_o} = \frac{\partial F^{ss}}{\partial g}\frac{\partial g}{\partial y_o} = \frac{\partial F^{ss}}{\partial g} \tag{99}
$$

Substituting (85) into (55) and evaluating (99) gives

$$
\frac{dF^{ss}}{dy_o} = \frac{w}{4\pi\mu_0}\int_{-\infty}^{\infty}\xi\Gamma(\xi,b)\left|B^s(\xi,b)\right|^2 d\xi, \tag{100}
$$

and from (96), (97) and (100) one obtains

$$
\frac{dF^{ss}}{dx_o} = \frac{jw}{4\pi\mu_0}\int_{-\infty}^{\infty}\xi\Gamma(\xi,b)\left|B^s(\xi,b)\right|^2 d\xi, \tag{101}
$$

Using the parameters given in Table 1 the lift and drag force on the EDW as a function of translational velocity for the case when $\omega_e = 0$ and $v_y = 0$ is shown in Figure 14. The stiffness coefficients obtained using (95) is shown in Figure 15. The stiffness coefficients k_{yy} is positive for increase in translational velocity. This stiffness coefficient is acting similar to the mechanical spring; when the rotor is pushed close to the conductive plate, it will be pushed back because
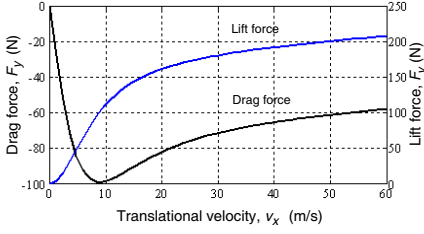
Figure 14. Electrodynamic lift, F_y, and drag force, F_x, as a function of translational velocity at $(\omega_e, v_y) = (0,0)$. As $\omega_e = 0$ the tangential force is a drag force.
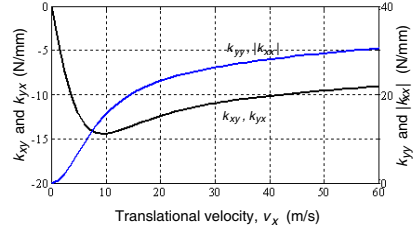

Figure 15. The electrodynamic stiffness coefficients as a function of translational velocity at $g = 10\,\mathrm{mm}$ and $\omega_e = 0\,\mathrm{rads}^{-1}$, $v_y = 0\,\mathrm{ms}^{-1}$.
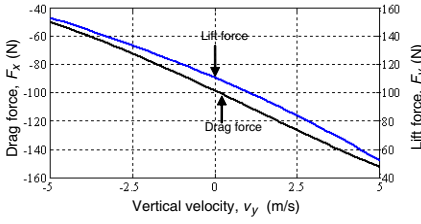

Figure 16. Lift, F_y and drag force, F_x versus EDW heave velocity, for $(\omega_e, v_x) = (0, \, 10\,\mathrm{ms}^{-1})$.
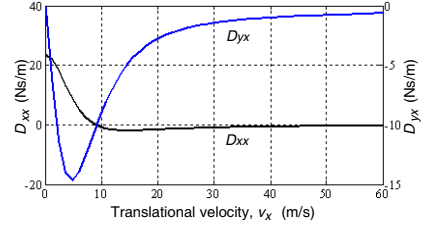

Figure 17. The electrodynamic damping terms, D_{xx} and D_{yx}.

of a positive stiffness, a necessary condition for stability. The stability exists in the direction of positive stiffness if the reaction force acts to oppose perturbatory displacements [46]. The negative stiffness, k_{xy}, is a consequence of the drag force decreasing with height.

Figure 16 shows that for small changes in the EDW heave velocity the variation in the lift and drag force is linear. Figure 17 and Figure 18 show the EDW vertical and horizontal damping characteristics calculating using (89). The damping coefficient D_{xx} is positive at velocities below the peak of the drag force and then becomes negative with further increase in translational velocity. In terms of energy, the positive damping means taking away energy from the system whereas negative damping refers to adding energy to the system [47]. The damping coefficient D_{yx} is always negative and peaks at a low translational speed. Since the lift force increases with increase in v_x (see Figure 14), energy is being added to the system, hence, the damping coefficient D_{yx} is negative.

Both drag and lift force are decreasing with an increase in the EDW heave velocity (see Figure 16), the energy is being taken away from the system. Therefore, the damping coefficients D_{xy} and D_{yy} are both positive. The vertical damping coefficient, D_{yy} decreases and becomes almost zero with an increase in translational velocity. However, the damping coefficient D_{xy} reaches a maximum value at peak drag force and then decreases with further increases in translational speed. These damping characteristics shown in Figure 18 agree with the calculations performed by Yoshida and Takakura [12], Urankar [13] in which no negative vertical damping D_{yy} was calculated.

For the case when $\omega_e \neq 0$ a slip will be present as defined by (1). Depending on the slip value the tangential force can be either a thrust or a drag force as shown in Figure 19. The lift and tangential force as function of slip and translational speed is shown in Figure 20 while Figure 21 shows the stiffness contour plots. The same stiffness relationships given by (95), (96) and (97) apply when $\omega_e \neq 0$. The cross coupled stiffness terms k_{xy}, k_{yx} become positive for positive slip values and therefore this should improve stability. The damping
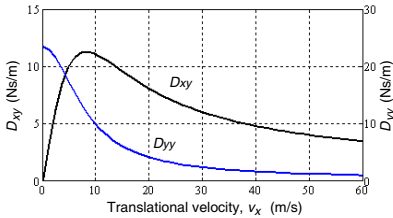

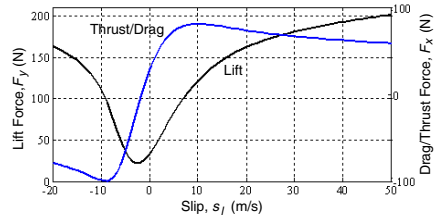**Figure 18.** The electrodynamic damping terms, D_{xy} and D_{yy}.

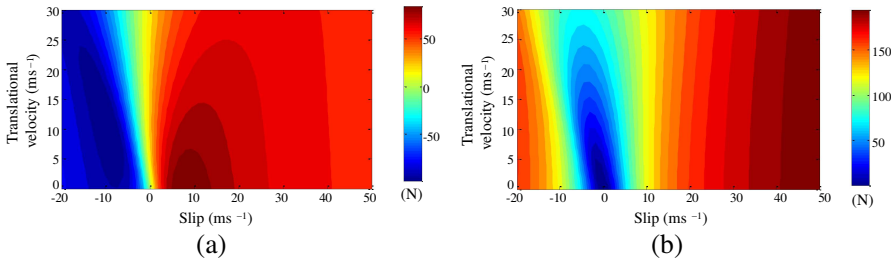**Figure 19.** Thrust (tangential) force and lift (normal) force as a function of slip when $v_x = 20\,\mathrm{ms}^{-1}$.

Figure 20. (a) Thrust force and (b) lift force as a function of slip and translational velocity at $g = 10\,\mathrm{mm}$ and $v_y = 0\,\mathrm{m/s}$.
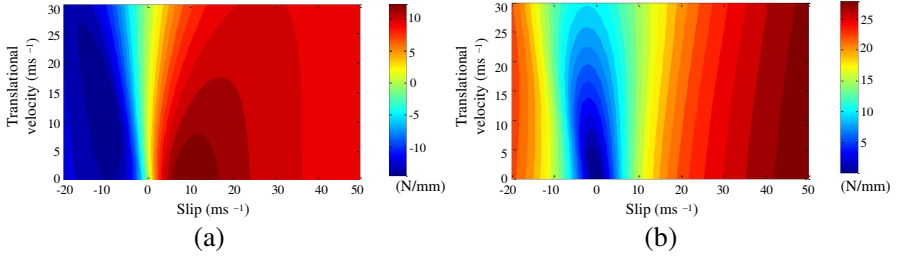
Figure 21. (a) The stiffness coefficients k_{xy} and k_{yx}, (b) the stiffness coefficients k_{yy} and $|k_{xx}|$ as a function of slip and translational velocity at $g = 10\,\text{mm}$ and $v_y = 0\,\text{m/s}$.
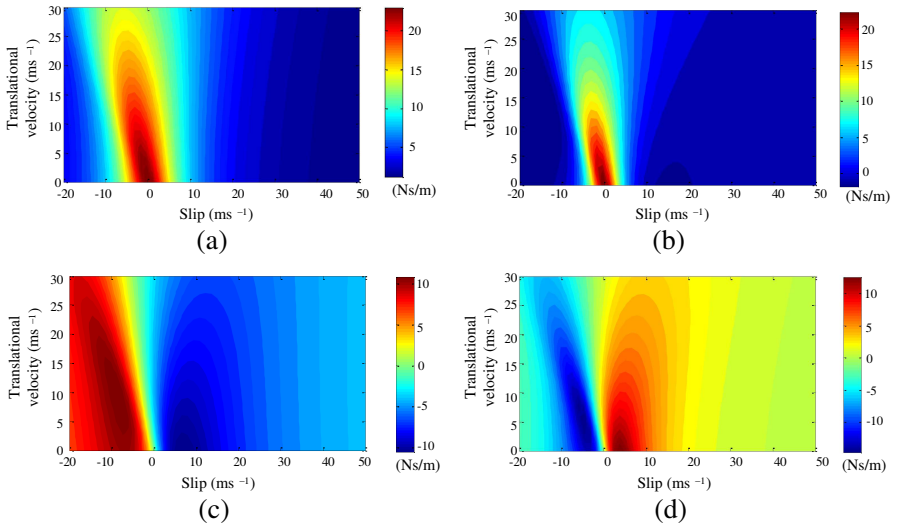

Figure 22. (a) Damping coefficient D_{yy}, (b) damping coefficient D_{xx}, (c) damping coefficient D_{xy} and (d) damping coefficient D_{yx} all as a function of slip and translational velocity at $g = 10\,\text{mm}$ and $v_y = 0\,\text{m/s}$.

relationships are shown in Figure 22. It can be noted that the vertical damping, D_{yy}, is always positive but decreases with slip value. Unlike in Figure 17, the horizontal damping coefficient, D_{xx}, becomes positive when both the translational and rotational speed are included. The magnitude of D_{xx} however decreases with increase in slip value as shown in Figure 22(b). The off-diagonal damping term D_{yx} is positive for positive slip values. Whereas the other off-diagonal damping term D_{yx} is negative when operating with thrust and therefore this term is
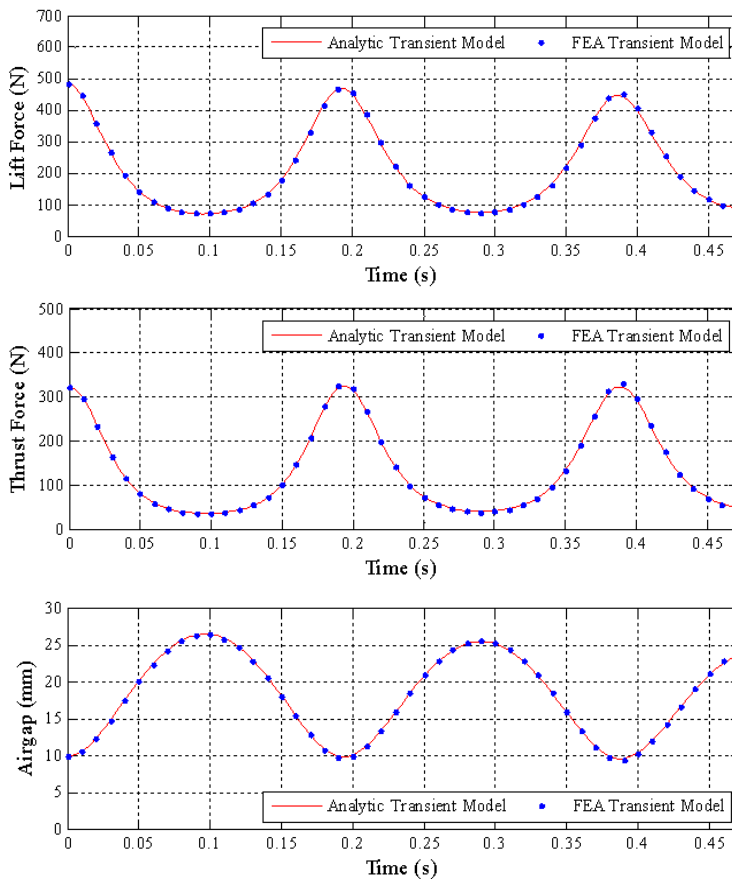
Figure 23. Lift, thrust and airgap plot comparison between the FEA transient model and analytical transient model when integrated with the *Matlab-Simmechanics* vehicle model.

likely to create instabilities. The decrease of the magnetic damping values at high slip values suggests that the inherent magnetic damping is insufficient and therefore active control of an electrodynamic maglev system is essential.

8. CONCLUSIONS

A 2-D analytic based steady-state eddy current model that incorporates heave and translational velocity as well as rotational motion has been derived. In addition, a dynamic eddy-current model

capable of reacting to continuous changes in input conditions has also been presented. The steady-state and transient eddy-current models were both incorporated into an electromechanical system in order to assess the calculation accuracy of the steady-state model when heave velocity is included. An electrodynamic wheel (Halbach rotor) was used as the source field. The simulation results indicate that the inclusion of the heave velocity, v_y, into a steady-state model creates a means for feedback in the electromechanical system thereby enabling the steady-state based force calculations to quite accurately track the dynamic behavior. The electromechanical simulation time is greatly reduced when the eddy current forces are computed from steady-state equations. Using the concept of reflected and transmitted fields the tangential and normal force equations were derived in a simplified form this enabled the exact damping and stiffness equations to be analytically derived.

9. ACKNOWLEDGMENT

APPENDIX A.

The analytic based electromechanical transient eddy current model with continuous time varying capabilities presented in Section 4 and Section 5 was validated by comparing it with a transient 2D FEA model that was also integrated into the electromechanical system described in Section 5 [33]. The transient FEA model utilized a fictitious current sheet [5] approach to model the Halbach rotor. The FEA model was developed in *COMSOL* v3.5 and integrated into the *Matlab* SimMechanics$^{\text{TM}}$ model environment utilizing *Matlab* s-functions. The comparison is made by using the parameters given in Table 1 except that an equivalent time-varying current sheet value $J_z = 1.1814 \times 10^6 \, \text{Am}^{-1}$ was used to model the source [5]. The 'vehicle' was started with initial conditions: airgap $g_o = 10 \, \text{mm}$, translational velocity, $v_{xo} = 10 \, \text{ms}^{-1}$ and angular velocity, $\omega_{mo} = 400 \, \text{rads}^{-1}$. These initial conditions result in a positive slip $s_l = 10 \, \text{ms}^{-1}$. The comparison between the lift force, thrust force and the air-gap are illustrated in Figure 23. An excellent agreement between the FEA model and the analytic based transient model for a continuously changing input condition was obtained. The integrated simulation approach developed between the transient FEA model and SimMechanics$^{\text{TM}}$ vehicle model was extremely time intensive. For instance, to obtain the result shown

in Figure 23 took approximately 2 weeks. However, the computational time using the analytic based transient eddy current model could be completed within a few minutes.

REFERENCES

1. Bohn, G. H. and G. Steinmetz, "The electromagnetic levitation and guidance technology of the 'transrapid' test facility Emsland," *IEEE Transactions on Magnetics*, Vol. 20, No. 5, 1666–1671, Sep. 1984.

2. Davey, K. R., "Designing with null flux coils," *IEEE Transactions on Magnetics*, Vol. 33, No. 5, 4327–4334, Sep. 1997.

3. Karoly, K., M. K. Volus, and K. Robert, "Design considerations for the hunting and braking performance of Maglev vehicle utilizing permanent magnet EDS levitation system," *MAGLEV 2006*, 363–370, Dresden, Germany, 2006.

4. Bird, J. and T. A. Lipo, "Characteristics of an electrodynamic wheel using a 2-D steady-state model," *IEEE Transactions on Magnetics*, Vol. 43, 3395–3405, Aug. 2007.

5. Bird, J. and T. A. Lipo, "Calculating the forces created by an electrodynamic wheel using a 2D steady-state finite element model," *IEEE Transactions on Magnetics*, Vol. 44, No. 3, 365–372, Mar. 2008.

6. Halbach, K., "Design of permanent multipole magnets with oriented rare earth cobalt material," *Nucl. Instr. and Meth.*, Vol. 187, 1–10, 1980.

7. Shute, H. A., J. C. Mallinson, D. T. Wilton, and D. J. Mapps, "One-sided fluxes in planar, cylindrical, and spherical magnetized structures," *IEEE Transactions on Magnetics*, Vol. 36, No. 2, 440–451, 2000.

8. Ravaud, R. and G. Lemarquand, "Discussion about the magnetic field produced by cylindrical halbach structures," *Progress In Electromagnetics Research B*, Vol. 13, 275–308, 2009.

9. Rote, D. M. and Y. Cai, "Review of dynamic stability of repulsive-force maglev suspension systems," *IEEE Transactions on Magnetics*, Vol. 38, No. 2, 1383–1390, Mar. 2002.

10. Davis, L. C. and D. F. Wilkie, "Analysis of motion of magnetic levitation systems: Implications for high-speed vehicles," *Jour. of Appl. Phy.*, Vol. 42, No. 12, 4779–4793, Nov. 1971.

11. Baiko, A. V., K. E. Voevodskii, and V. M. Kochetkov, "Vertical

unstable stability of electrodynamic suspension of high speed ground transport," *Cryogenics*, Vol. 20, No. 5, 271–276, May 1980.

12. Yoshida, K. and M. Takakura, "Magnetic damping and stiffness coefficients in superconducting maglev system with sheet guideways," *Electr. Eng. Japan*, Vol. 99, No. 12, 797–804, 1979.

13. Urankar, L., "Intrinsic damping in basic magnetic levitation systems with a continuous sheet track," *Siemens Forschungs and Entwicklungsberichte*, Vol. 5, No. 2, 110–119, 1996.

14. Yamada, T., M. Iwamoto, and T. Ito, "Magnetic damping force in inductive magnetic levitation system for high-speed trains," *Electr. Eng. Japan*, Vol. 94, No. 1, 49–54, 1974.

15. Iwamoto, M., T. Yamada, and E. Ohno, "Magnetic damping force in electrodynamically suspended trains," *IEEE Transactions on Magnetics*, Vol. 10, No. 3, 458–461, 1974.

16. Fujiwara, S., "Damping characteristics of the repulsive magnetic levitation vehicle," *Japanese Railway Technial Res. Inst., Quart. Rep.*, Vol. 21, No. 1, 49–52, 1980.

17. Higashi, K., S. Ohashi, H. Ohsaki, and E. Masada, "Magnetic damping of the electrodynamic suspension-type superconducting levitation system," *Electr. Eng. Japan*, Vol. 127, No. 2, 1015–1023, 1999.

18. Ooi, B. T., "Electromechanical stiffness and damping coefficients in the repulsive magnetic levitation system," *IEEE Trans. Power App. Syst.*, Vol. 95, No. 3, 936–943, May–Jun. 1976.

19. Takano, I. and H. Ogiwara, "Magnetic damping characteristics of magnetically suspended ultrahigh-speed vehicles," *Electr. Eng. Japan*, Vol. 98, No. 5, 14–23, Sep. 1978.

20. Kratki, N. and K. Oberretl, "Ausgleichsvorgiinge und schwingungen beim elektrodynamischen magnetkissen-system," *Archiv fur Elektrotechnik*, Vol. 57, 59–64, 1975.

21. He, J. L. and H. T. Coffey, "Magnetic daming forces in figure-eight-shaped null-flux coil suspension systems," *IEEE Transactions on Magnetics*, Vol. 33, No. 5, 4230–4232, Sep. 1997.

22. Zhu, S., Y. Cai, D. M. Rote, and S. S. Chen, "Magnetic damping for maglev," *Shock and Vibration*, Vol. 5, 119–128, 1998.

23. Smythe, W. R., *Static & Dynamic Electricity*, 5th Edition, 1989.

24. Bird, J. and T. A. Lipo, "Modeling the 3-D rotational and translational motion of a Halbach rotor above a split-sheet guideway," *IEEE Transactions on Magnetics*, Vol. 45, No. 9, 3233–3242, Sep. 2009.

25. Goldstein, H., C. Poole, and J. Safko, *Classical Mechanics*, 2002.

26. Paudel, N. and J. Z. Bird, "General 2D steady-state force and power equations for a traveling time-varying magnetic source above a conductive plate," *IEEE Transactions on Magnetics*, Vol. 48, No. 1, 95–100, Jan. 2012.

27. Sankaran, R., K. P. P. Pillai, and D. A. Muraleedharan, "Transient performance of linear induction machines following reconnection of supply," *Proc. IEE*, Vol. 126, No. 10, 979–983, 1979.

28. Paudel, N., J. Z. Bird, S. Paul, and D. Bobba, "Modeling the dynamic suspension behavior of an eddy current device," *Energy Conversion Congress and Exposition (ECCE)*, 1692–1699, 2011.

29. Yamamura, S., *Theory of Linear Induction Motors*, University of Tokyo Press, 1979.

30. Rodger, D. and J. F. Eastham, "Dynamic behavior of linear induction machines in the heave mode," *IEE Trans. Vehicular Technology*, Vol. 31, No. 2, 1982.

31. Paudel, N., S. Paul, and J. Z. Bird, "General 2-D transient eddy current force equations for a magnetic source moving above a conductive plate," *Progress In Electromagnetics Research B*, Vol. 43, 255–277, 2012.

32. Rodger, D., P. J. Leonard, and T. Karaguler, "An optimal formulation for 3D moving conductor eddy current problems with smooth rotors," *IEEE Transactions on Magnetics*, Vol. 26, No. 5, 2359–2363, Sep. 1990.

33. Paudel, N., "Dynamic suspension modeling of an eddy-current device: An application to MAGLEV," Ph.D. Thesis, Electrical and Computer Engineering, University of North Carolina at Charlotte, Charlotte, NC, 2012.

34. Polyanin, A. D. and A. V. Manzhirov, *Handbook of Mathematics for Engineers and Scientists*, Chapman & Hall, 2007.

35. Freeman, E. M. and C. Papageorgiou, "Spatial Fourier transforms: A new view of end effects in linear induction motors," *Proc. IEE*, Vol. 125, No. 8, 747–753, Aug. 1978.

36. Rao, S. S., *Mechanical Vibrations*, 2nd Edition, Addison-Wesley, Reading, Massachusetts, 1990.

37. Xia, Z. P., Z. Q. Zhu, and D. Howe, "Analytical magnetic field analysis of Halbach magnetized permanent-magnet machines," *IEEE Transactions on Magnetics*, Vol. 40, No. 4, 1864–1872, Jul. 2004.

38. Atallah, K., D. Howe, P. H. Mellor, and D. A. Stone, "Rotor loss in permanent-magnet brushless AC machines," *IEEE Trans. Ind. Appl.*, Vol. 36, No. 6, 1612–1618, Nov.–Dec. 2000.

39. Zhu, S., Y. Cai, D. M. Rote, and S. S. Chen, "Magnetic damping for maglev," ANL/ET/CP-82419, CONF-9411194–2, Energy Technology Division, Argonne National Laboratory, 1995.

40. Gillespire, T. D., *Fundamentals of Vehicle Dynamics*, Society of Automotive Engineers, Inc., 1992.

41. Moon, F. C., *Superconducting Levitation: Applications to Bearings and Magnetic Transportation*, WILEY-VCH Verlag GmbH & Co. KGaA, 2004.

42. Brown, J. W. and R. V. Churchill, *Complex Variables and Applications*, 6th Edition, McGraw-Hill Inc., New York, 1996.

43. Earnshaw, S., "On the nature of the molecular forces which regulate the constitution of the luminferous ether," *Transactions Camb. Phil. Soc.*, Vol. 7, 97–112, 1842.

44. Di Puccio, F., A. Musolino, R. Rizzo, and E. Tripodi, "A self-controlled maglev system," *Progress In Electromagnetics Research M*, Vol. 26, 187–203, 2012.

45. Di Puccio, F., R. Bassani, E. Ciulli, A. Musolino, and R. Rizzo, "Permanent magnet bearings: Analysis of plane and axisymmetric v-shaed element design," *Progress In Electromagnetics Research M*, Vol. 26, 205–223, 2012.

46. Post, R. F. and D. D. Ryutov, "Ambient-temperature passive magnetic bearings: Theory and design equations," *6th International Symposium on Magnetic Bearings*, Cambridge, Massachusetts, 1998.

47. Higashi, K., S. Ohashi, H. Ohsaki, and E. Masada, "Damping mechanism of the superconducting electrodynamic suspension system," *Nonlinear Electromagnetic Systems: Proceedings of the International IOS Press*, 1996.